Cdc42 negatively regulates endocytosis during apical membrane maintenance in live animals

Akiko Shitara[a,†], Lenka Malec[a], Seham Ebrahim[a], Desu Chen[a,b], Christopher Bleck[c], Matthew P. Hoffman[d], and Roberto Weigert[a,e,*]

[a]Laboratory of Cellular and Molecular Biology, Center for Cancer Research, National Cancer Institute, [c]Electron Microscopy Core Facility, National Heart, Lung, and Blood Institute, [d]Matrix and Morphogenesis Section and [e]Intracellular Membrane Trafficking Section, National Institute of Dental and Craniofacial Research, National Institutes of Health, Bethesda, MD 20892; [b]College of Computer, Mathematical, and Natural Sciences, University of Maryland, College Park, MD 20742

ABSTRACT **Lumen establishment and maintenance are fundamental for tubular organs physiological functions. Most of the studies investigating the mechanisms regulating this process have been carried out in cell cultures or in smaller organisms, whereas little has been done in mammalian model systems in vivo. Here we used the salivary glands of live mice to examine the role of the small GTPase Cdc42 in the regulation of the homeostasis of the intercellular canaliculi, a specialized apical domain of the acinar cells, where protein and fluid secretion occur. Depletion of Cdc42 in adult mice induced a significant expansion of the apical canaliculi, whereas depletion at late embryonic stages resulted in a complete inhibition of their postnatal formation. In addition, intravital subcellular microscopy revealed that reduced levels of Cdc42 affected membrane trafficking from and toward the plasma membrane, highlighting a novel role for Cdc42 in membrane remodeling through the negative regulation of selected endocytic pathways.**

Monitoring Editor
Alpha Yap
University of Queensland

Received: Oct 4, 2018
Revised: Dec 6, 2018
Accepted: Dec 7, 2018

INTRODUCTION

Epithelial cells have two specialized surface domains, the basolateral and the apical, each with a distinct composition and function (Bryant and Mostov, 2008; Willenborg and Prekeris, 2011). In tubular organs such as the salivary and mammary glands, lung, kidney, pancreas, and intestine, the apical plasma membrane (APM) forms the lumens. These specialized areas of the cell are implicated in extensive protein, fluid, and electrolyte secretion and uptake, and therefore are subjected to constant remodeling (Masedunskas *et al.*, 2011b; Willenborg and Prekeris, 2011; Tepass, 2012). The establishment and maintenance of the APM are regulated by a complex signaling cascade controlled by the small GTPase Cdc42 (Etienne-Manneville, 2004; Melendez *et al.*, 2011). In its GTP-bound form, Cdc42 binds and activates PAR6, a member of the apical PAR polarity complex (PAR3–PAR6–aPKC), which together with the Crumbs (Crb–PALS–PATJ) and Scribble (Scrib–Dlg–Lgl) complexes dictate the positioning of the apical–basolateral border through the assembly of tight and adherens junctions (Bryant and Mostov, 2008). In addition, the polarity complexes regulate a series of downstream effectors, which coordinate the activation of both actin cytoskeleton and membrane trafficking, and are required for establishing and maintaining cell polarity (Etienne-Manneville, 2004; Melendez *et al.*, 2011).

The role of Cdc42 in regulating the homeostasis and establishment of the APM has been extensively investigated in Madin-Darby canine kidney (MDCK) cells grown in purified extracellular matrix components (Martin-Belmonte *et al.*, 2007; Jaffe *et al.*, 2008; Bryant *et al.*, 2010). The versatility of this experimental model has allowed the identification of a large number of molecules implicated in this process, and to tease out several details of this complex molecular machinery (Etienne-Manneville, 2004; Bryant and Mostov, 2008; Apodaca, 2010). In addition, substantial work has been performed in smaller multicellular organisms such as *Drosophila*, *Caenorhabditis*

This article was published online ahead of print in MBoC in Press (http://www.molbiolcell.org/cgi/doi/10.1091/mbc.E18-10-0615) on December 12, 2018.

A.S. and R.W. designed the experiments. A.S., L.M., and S.E. performed the experiments. A.S., L.M., and D.C. analyzed the data. C.B. performed EM experiments. M.P.H. provided contributions with the developmental experiments. A.S. and R.W. wrote the manuscript. All authors read and approved the final manuscript.

†Present address: Department of Pharmacology, Asahi University School of Dentistry, 1851-1 Hozumi, Mizuho, Gifu 501-0296, Japan.

*Address correspondence to: Roberto Weigert (weigertr@mail.nih.gov).

Abbreviations used: APM, apical plasma membrane; BLM, basolateral membrane; EM, electron microscopy; IC, intercellular canaliculi; IF, immunofluorescence; ISMic, intravital subcellular microscopy; SMG, submandibular salivary gland; TJ, tight junctions.

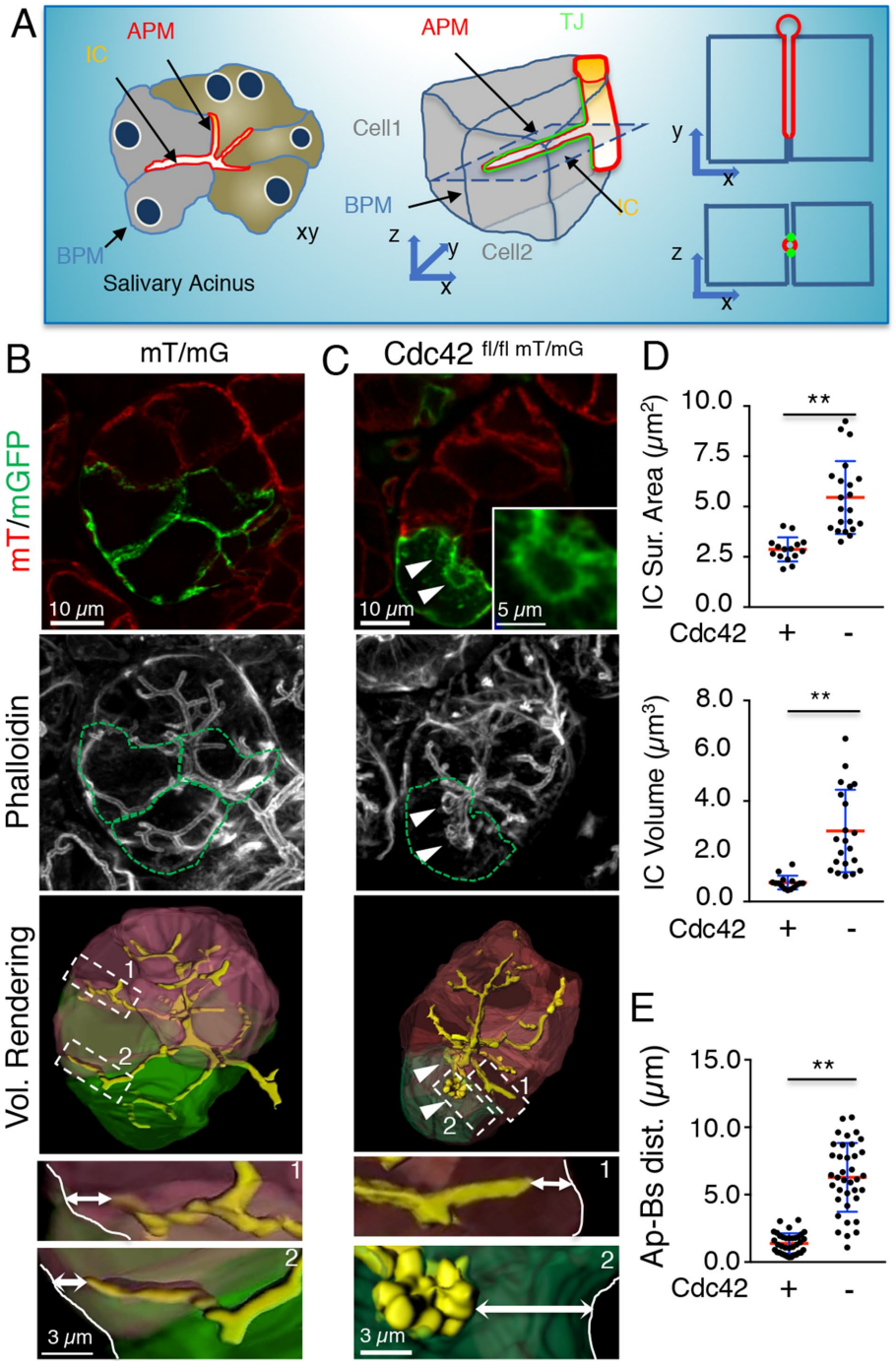

FIGURE 1: Cdc42 depletion induces luminal expansion of the IC in adult mice. (A) Diagram of the salivary glands acinus showing the structure of the IC formed by the APM of two adjacent cells. XY and XZ view of the canaliculi. Highlighted in green are the TJ. (B, C) mT/mG (B) or Cdc42$^{fl/fl\text{-}mT/mG}$ (C) mice were transfected with Adeno-Cre. After 3 wk the glands were excised, labeled with Alexa 647-phalloidin, and imaged by confocal microscopy, as described in *Materials and Methods*. Dashed green lines highlight the Cre-expressing cells. Arrowheads highlight the expanded ICs. Bottom panels feature the volume rendering of representative acini (Cre-positive cells highlighted in green, Cre-negative cells highlighted in red; see also Supplemental Movies S1 and S2). Double arrows highlight the distance between the tip of the IC and the basal PM. (D) Quantification of surface area and volume of IC in Cdc42$^{fl/fl\text{-}mT/mG}$ mice. Cre-negative (Cdc42^{+}) cells: surface area, 2.87 ± 0.59 μm^2; volume, 0.75 ± 0.27 μm^3, N = 15) and Cre-positive cells (Cdc42-; surface area: 5.45 ± 1.81 μm^2; volume, 2.81 ± 1.64 μm^3, N = 21). Data are means ± SD; N = number of IC from 11 acinar cells scored in four animals; **, $p < 0.01$, unpaired Student's t test. (E) Quantification of distance between the tip of the IC and the basal PM in Cre-negative (Cdc42^{+}; 1.38 ± 0.75 μm, N = 36) and Cre-positive (Cdc42–; 6.28 ± 2.55 μm, N = 37). Data are means ± SD; N = number of IC from 11 acinar cells from five animals; **, $p < 0.01$, unpaired Student's t test.

elegans, and zebrafish (Kamei *et al.*, 2006; Balklava *et al.*, 2007; Georgiou *et al.*, 2008; Pirraglia *et al.*, 2010). However, only a limited amount of work has been carried out in mammalian organisms (i.e., rodents). These studies, which took advantage of the ablation of Cdc42 in specific adult tissues such as the liver (van Hengel *et al.*, 2008), pancreas (Kesavan *et al.*, 2009), intestine (Melendez *et al.*, 2013), and inner ear (Ueyama *et al.*, 2014), showed a fundamental role of Cdc42 in regulating apical polarity, although they did not focus on the characterization of its role in regulating membrane remodeling and trafficking.

Here, we used a combination of intravital subcellular microscopy (ISMic), a light microscopy-based technique that enables imaging the dynamics of intracellular structures in live animals (Masedunskas *et al.*, 2011a, 2013; Pittet and Weissleder, 2011; Weigert *et al.*, 2013; Milberg *et al.*, 2014), and indirect immunofluorescence to examine the role of Cdc42 in controlling maintenance and formation of the intercellular canaliculi (IC) in the acinar cells of the submandibular salivary glands (SMGs) in live mice. These structures are narrow tubes, formed by the APM of two adjacent acinar cells (Figure 1), which constitute a network spanning throughout the secretory acini (Figure 1A) and connected to a central canaliculus that leads to the intercalated ducts (Tamarin and Sreebny, 1965). The IC play a fundamental role in the physiology of the salivary glands because they are the site where protein and fluid secretion occur. Cdc42 was ablated in either adult mice or on embryonic day 15. We found that reduction in the levels of Cdc42 in adult mice resulted in the involution of the IC, which progressively retracted from the basal border and underwent significant expansions. On the other hand, in neonatal mice, the lack of Cdc42 resulted in the complete inhibition of the formation of the IC. In parallel, we observed a massive stimulation of endocytic trafficking, thus suggesting a scenario in which Cdc42 negatively regulates endocytosis during maintenance and establishment of membrane polarity.

RESULTS AND DISCUSSION

Cdc42 depletion causes the expansion of the IC in adult mice

To define the role of Cdc42 in maintaining the homeostasis of luminal structures in live adult mice, we used a Cre/loxP approach to deplete Cdc42 from the SMG acinar cells. Cdc42 floxed mice (Chen *et al.*, 2006) were crossed with the Cre-recombinase (Cre) reporter mouse strain Rosa$^{mT/mG}$ (mTmG;

Muzumdar *et al.*, 2007), as shown in Supplemental Figure S1A ($Cdc42^{fl/fl\text{-}mT/mG}$). The mT/mGFP probe provides a marker for both Cre expression and visualization of the plasma membrane (PM), as previously described (Masedunskas *et al.*, 2011a; Milberg *et al.*, 2017). Cre expression was induced in 5–10% of the acinar cells by the injection of a Cre-expressing adenovirus (Adeno-Cre) into the submandibular main duct (Sramkova *et al.*, 2009; Milberg *et al.*, 2017). In $Cdc42^{fl/fl\text{-}mT/mG}$ mice, 3–4 wk after the adenovirus injection, Cre-expressing cells exhibited large vacuolar structures labeled with membrane-targeted GFP (mGFP) and contiguous to the APM (Figure 1C, top panel, arrowheads, and inset). F-actin labeling, which highlights the APM, revealed that these structures were the result of IC expansion (Figure 1C, middle panel, arrowheads, and inset). We also found that the expanded IC were primarily observed in cells with lower levels of Cdc42, as assessed by immunofluorescence (Supplemental Figure S1B). Z-stacks and volume rendering of the acini further confirmed that the APM bulged toward the interior of Cdc42-depleted cells (Figure 1C, bottom panel, and Supplemental Movie S1). In contrast, no changes were observed in either Cre-negative cells (Figure 1C) or Cre-positive cells in mTmG mice that were used as additional controls (Figure 1B and Supplemental Movie S1). Quantitative analysis showed that Cdc42-depletion resulted in the 1) increase of both surface area and volume of the APM with respect to control cells (Figure 1D); and 2) shortening of the IC length (Figure 1E), as shown by measuring the distance between the tip of the IC and the basal PM, which suggests a repositioning of the apical–lateral border (Figure 1, B and C, bottom panels). Interestingly, the apical–lateral border was altered regardless if it was shared between one or two cells lacking Cdc42 (Supplemental Figure S1C). Finally, depletion of the small GTPases RhoA and Rac1 did not have any effect on the morphology of the IC, thus suggesting a specific role for Cdc42 in their maintenance (Supplemental Figure S1D).

Cdc42 depletion leads to loss of PAR6 and F-actin at the APM

We reasoned that changes in the morphology of the IC in Cdc42-depleted cells could be the result of a defect in the maintenance of cell polarity. Therefore, we investigated the recruitment of the PAR polarity complex on the salivary glands APM. In cell culture and in small organisms this complex has been shown to regulate various functions such as establishment and maintenance of polarity, cytoskeletal assembly, tight junction (TJ) formation, and positioning of the apical–lateral border (Suzuki and Ohno, 2006; Morais-de-Sá *et al.*, 2010; Walther and Pichaud, 2010; Tepass, 2012). We found that in the IC of Cdc42-depleted acinar cells, the levels of PAR6, one of the main components of the polarity complex that is directly activated by Cdc42 (Joberty *et al.*, 2000), were significantly reduced (Figure 2A), together with the levels of F-actin, which were not affected at the basolateral membrane (BLM; Figure 2A). The levels of ZO-1, one of the components of the TJ, were also reduced at the IC in Cre-expressing cells (Supplemental Figure S2A; Stevenson *et al.*, 1986), whereas the levels and the organization of both E-cadherin, a marker of the adherens junctions (Supplemental Figure S2B), and nonmuscle myosin IIA (Supplemental Figure S2C) were not perturbed. Next, we checked whether both cell polarity and structural integrity were maintained in the expanded IC. We found that the APM and the BLM did not mix, as shown by staining the acinar cells for the two well-established salivary markers aquaporin 5 (AQP5) and the Na^+-K^+-Cl^- cotransporter 1 (NKCC1; Figure 2C; O'Grady *et al.*, 1987; Matsuzaki *et al.*, 1999). Studies in other experimental systems have shown that down-regulation of Cdc42 inhibits the formation of apical lumens and leads to the accumulation of large intracellular vacuoles (Martin-Belmonte *et al.*, 2007; Kesavan *et al.*, 2009; Sakamori *et al.*, 2012). To confirm that the structures observed in salivary acinar cells were indeed derived from the ICs, we retroinjected low molecular weight fluorescent dextran into the main salivary duct in the anesthetized mice and imaged its delivery to the ICs by ISMic (Masedunskas *et al.*, 2011a). We showed that in Cdc42-depleted cells, the enlarged ICs were still functionally connected to the main ductal system and, in addition, that paracellular integrity was not affected (Figure 2D, Supplemental Figure S2D, and Supplemental Movie S2).

Membrane trafficking is altered in Cdc42-depleted cells

On the basis of the increase in the surface area of the ICs, we hypothesized that their expansion could be the result of an imbalance in membrane trafficking toward and from the APM. Consistent with this idea, we found that the cytoplasm of Cdc42-depleted cells contained GFP-labeled vesicular structures with apparent diameters varying from 0.5 to 2.5 µm. These vesicles were not detected in control cells (Figure 3, A, arrows, and B). Interestingly, we observed large GFP-containing vesicles in the subapical area that occasionally generated tubular structures (Figure 3B, inset). Indirect immunofluorescence revealed that a subpopulation of vesicles smaller than 1.5 µm was endosomal in nature, as it was labeled by the early endosomal marker EEA1 (25 ± 6%, Av. ± SEM, $N = 3$ animals, 44 cells, 401 vesicles; Figure 3C) and only occasionally with the small GTPase Rab11a (5.5 ± 2.8%, Av. ± SEM, $N = 3$ animals, 42 cells, 527 vesicles; Figure 3D), which has been previously shown to label the apical recycling endosomes and to control APM maintenance by regulating membrane trafficking from the Golgi apparatus and the early apical endosomes (Balklava *et al.*, 2007; Winter *et al.*, 2012; Bai and Grant, 2015). Depletion of Cdc42 did not alter the number, size, and cellular distribution of the EEA1-positive early endosomes (Figure 3C) or the Rab11-positive compartments (Figure 3D). The remaining GFP-labeled vesicles were not labeled by makers such as LAMP1 (lysosomes), TGN46 (*trans*-Golgi network), GM130 (Golgi), VAMP4 (post-Golgi), or LC3 (autophagosomes; unpublished data).

To reveal the direction of trafficking of the GFP-labeled membranes in Cdc42-depleted cells, we used ISMic. These vesicles were very dynamic (Supplemental Movie S3) and they were transported toward several locations throughout the cells. We identified various patterns: 1) vesicles generated from the basolateral membranes and directed toward the center of the cell (Figure 3E, I) or the APM (Figure 3E, II); 2) vesicles directed to the APM (Figure 3E, III); 3) vesicles that fused or departed from large vesicles localized in the subapical areas (Figure 3E, IV); and 4) vesicles generated from the APM and fusing with the lateral domains (Figure 3E, V). These patterns were observed regardless of whether the cells were under basal conditions or stimulated to secrete proteins via β-adrenergic–dependent regulated exocytosis. Owing to the temporal and spatial limitation of light microscopy, we were not able to always visualize the initial steps in the internalization, and because the time-lapse images were acquired in a single focal plane, we could not track the vesicles for long distances, thus making it difficult to provide a quantitation of the frequency of these events. Nonetheless, these results strongly suggest that the expansion of the ICs could be linked to increased endocytic trafficking that delivers an excess of membranes to both the APM and the lateral membranes.

Notably, we ruled out that the IC expansion was due to an imbalance between regulated exocytosis of the large secretory granules and the subsequent compensatory endocytosis (Masedunskas *et al.*, 2011b). This conclusion was supported by two findings. First,

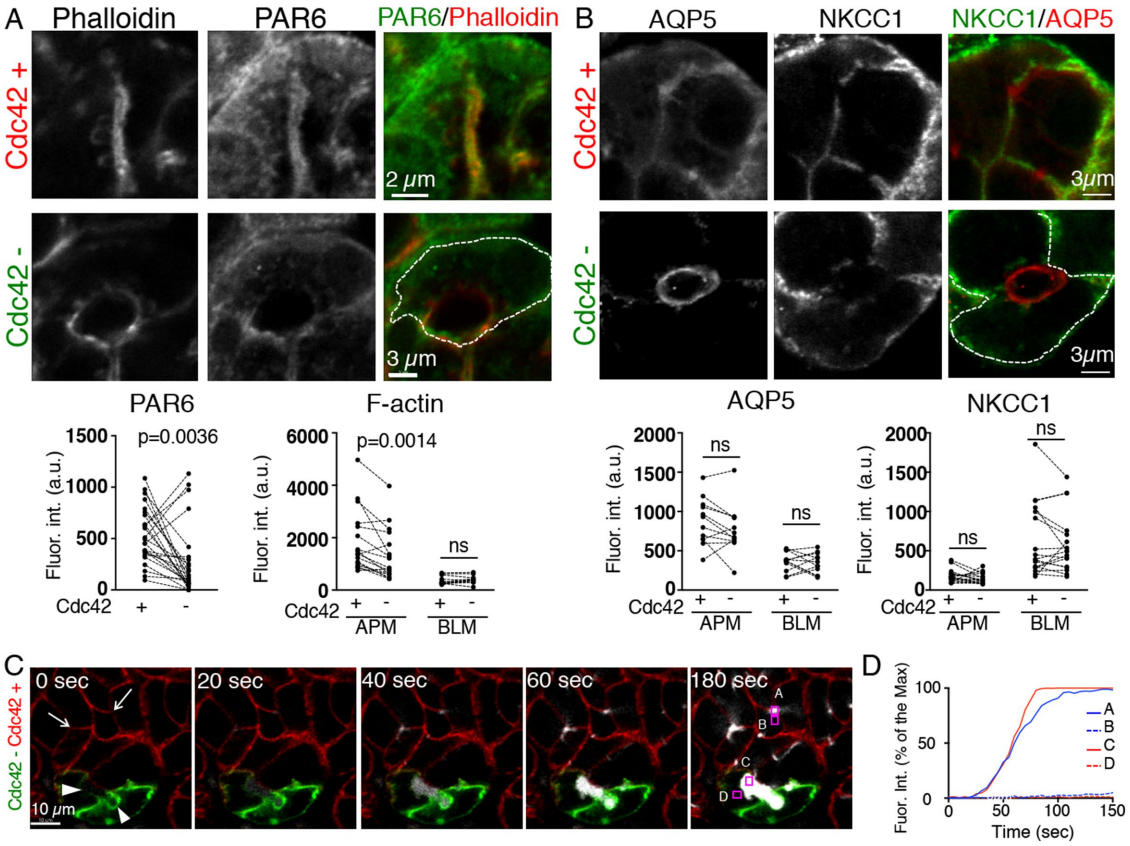

FIGURE 2: Cdc42-depletion results in loss of PAR6 and F-actin at the APM without altering polarity and junction permeability. (A, B) Cdc42$^{fl/fl\text{-}mT/mG}$ mice were transfected with Adeno-Cre and processed for immunofluorescence as described in the legend to Figure 1. Samples were labeled with iFluor 405-phalloidin (A, red) and an antibody against PAR6 (A, green) or with antibodies against AQP5 (B, red) and NKCC1 (B, green). Dotted lines outline the Cre-expressing cells. Graphs show the analysis of the levels of PAR6 (A), F-actin (A), AQP5 (B), and NKCC1 (B) in Cre-expressing (Cdc42^{-}) and Cre-nonexpressing (Cdc42^{+}) cells. (PAR6, $N = 25$ ICs, 11 acinar cells from three animals; F-actin, $N = 17$ APM and BLM, 12 acinar cells from four animals; AQP5, $N = 12$ APM and BLM, 9 acinar cells from three animals; and NKCC1, $N = 17$ APM and BLM, 17 acinar cells from five animals). ns = not significant, paired *t* test. (C, D) Three kDa Cascade Blue Dextran (White) was retrodiffused into the Wharton's duct of anesthetized Cdc42$^{fl/fl\text{-}mT/mG}$ mice after 3 wk from Adeno-Cre transfection. (C) The SMGs were exposed and imaged by ISMic. Time 0 represents the point at which dextran is detected in IC. Arrow and arrowhead in time 0 shows normal IC and expanded IC, respectively (C and Supplemental Movie S2). (D) Quantification of dextran fluorescence intensity within (A, C) and outside (B, D) in Cre-negative cells (A, B) and Cre-positive cells (C, D). Graph shows a representative experiment.

Cdc42 depletion in acinar cells did not affect the β-adrenergic receptor-dependent fusion of the secretory granules with the IC, although it delayed their integration into the APM (Supplemental Figure S3, A and B, and Supplemental Movie S4); this finding is consistent with a reduction in the levels of F-actin recruited on the granules (Supplemental Figure S3C), which control this process in vivo, as we reported (Masedunskas *et al.*, 2011a; Milberg *et al.*, 2017). Second, the integration of the secretory granules did not result in a further expansion of the IC, indicating a rapid retrieval of the granular membranes via compensatory endocytosis (Supplemental Movie S4; Sramkova *et al.*, 2009).

Cdc42 depletion impairs the formation of IC postnatally

In other model systems, it has been shown that maintenance and formation of the epithelial lumen share common mechanisms (Joberty *et al.*, 2000; Rojas *et al.*, 2001; Suzuki and Ohno, 2006). Therefore, we investigated whether Cdc42 controls the development of the IC in salivary acinar cells and negatively regulates endocytosis under these conditions. To this end, we crossed the Cdc42$^{fl/fl\text{-}mT/mG}$ mouse with a strain that expresses Cre under the control of the salivary gland–specific AQP5 promoter (ACID-Cre), which is activated in both acinar and intercalated duct cells at embryonic day 15 (Supplemental Figure S4, A and B; Flodby *et al.*, 2010). Although the animals were viable, we measured a significant loss in body weight (Supplemental Figure S4C), and no significant differences were observed in the organization of salivary tissues (Supplemental Figure S4D). In the acinar cells of adult Cdc42$^{-/-}$ mice, the levels of Cdc42 were reduced by 50%, as shown by quantitative immunofluorescence (Supplemental Figure S4E).

First, we determined the kinetics of formation of the IC in acinar cells, a process that is completed after birth (Tucker, 2007). In control animals, central luminal structures were observed at postnatal day 1 (P1), whereas the IC were not developed yet (Figure 4A). At P5 the IC began to sprout from the central lumen and to extend toward the basal membranes of the acini. At P15 they were fully developed and comparable to adult weaned mice (Figure 4, A and B, top panels, arrowheads, and Supplemental Movie S5). On the other hand, in Cdc42-depleted acini, the IC did not sprout from the central lumens. At P15 and in adult mice we observed one or two vacuolar-like structures within the same acinus (Figure 4, A and B,

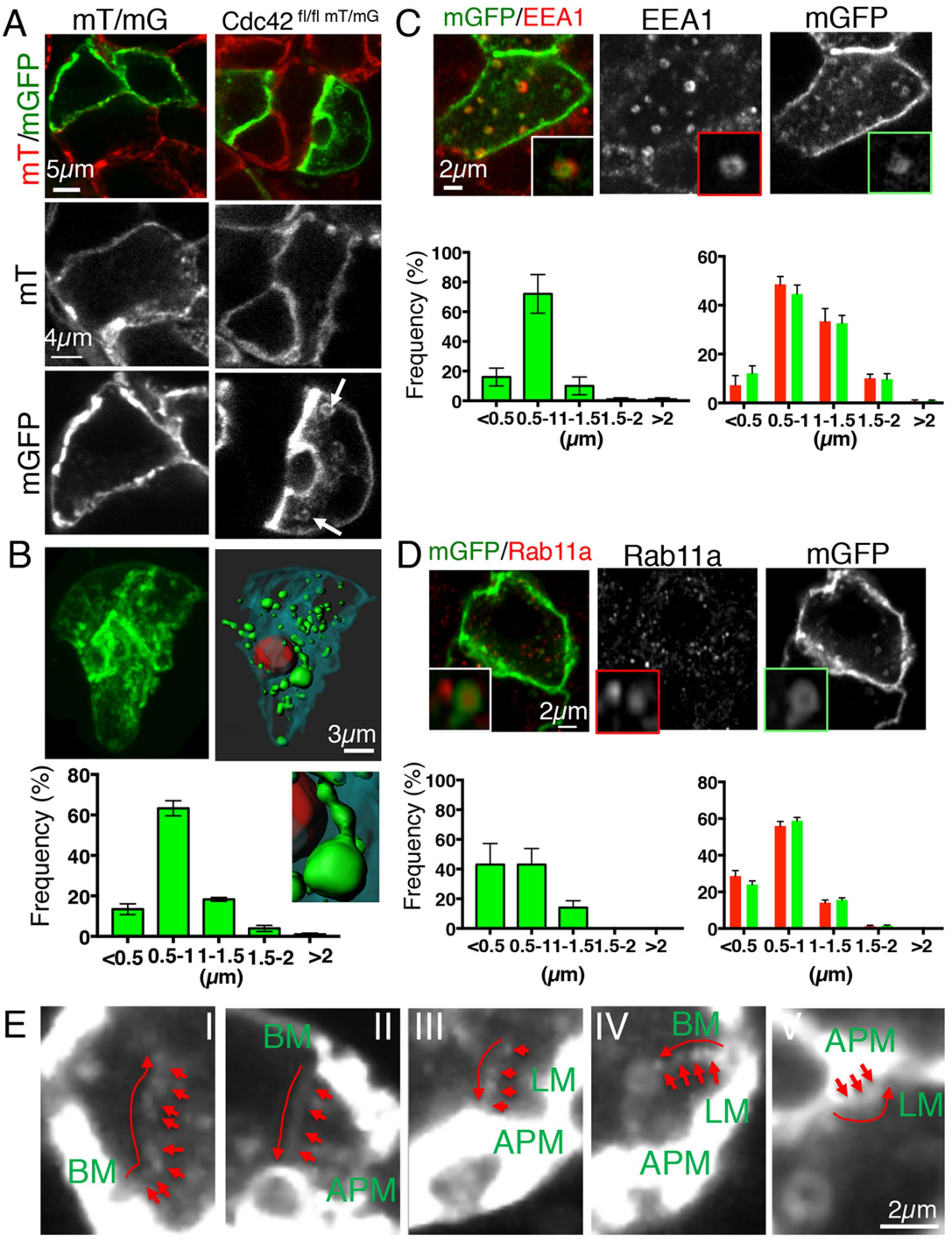

FIGURE 3: Membrane trafficking was altered in Cdc42-depleted cells. (A–E) mT/mG (A, left panel) or Cdc42$^{fl/fl\text{-}mT/mG}$ (A, right panel, B–E) mice were transfected with Adeno-Cre, as described in *Materials and Methods*. After 3 wk, the glands were excised and processed for immunofluorescence (A–D) or imaged by ISMic (E). (A–D) Excised glands were left untreated (A, B) or labeled with antibodies against EEA1 (C) or Rab11a (D). (A, B) Confocal images of single sections (A, arrows label mGFP-positive vesicles) or Z-stacks (B, cyan BLM, red APM, green vesicles; inset shows a membranous tubule forming from a large vesicle). Graph in B shows the size distribution of the mGFP-positive vesicles in the cells ($N = 619$ vesicles, in four animals; data are means ± SEM). (C, D) Colocalization between mGFP vesicles (green) and EEA1 (C, red) or Rab11a (D, red). Quantification of the size distribution of mGFP vesicles that colocalize with either EEA1 (C, left graph, $N = 351$ vesicles in three animals) or Rab11a (D, left graph, $N = 48$ vesicles in three animals). Quantification of the size distribution of either EEA1 (C, right graph) or Rab11A (D, right graph) vesicles in Cre-positive (green bars) and Cre-negative (red bars; EEA1, $N = 619$ vesicles in four animals; Rab11a, $N = 92$ vesicles in three animals). Data are means ± SEM. (E) ISMIc of Cre-positive cells. mGFP-labeled vesicles were tracked, as described in *Materials and Methods*. Each panel shows an overlay of different time points (see Supplemental Movie S3). Arrows point to the trajectory of selected vesicles that traffic from the basal membrane (BM) to the center of the cell (I), the BM to the APM (II), the center of the cell to the APM (III), the BM to a large vesicle (IV), and the APM to the lateral membrane (LM).

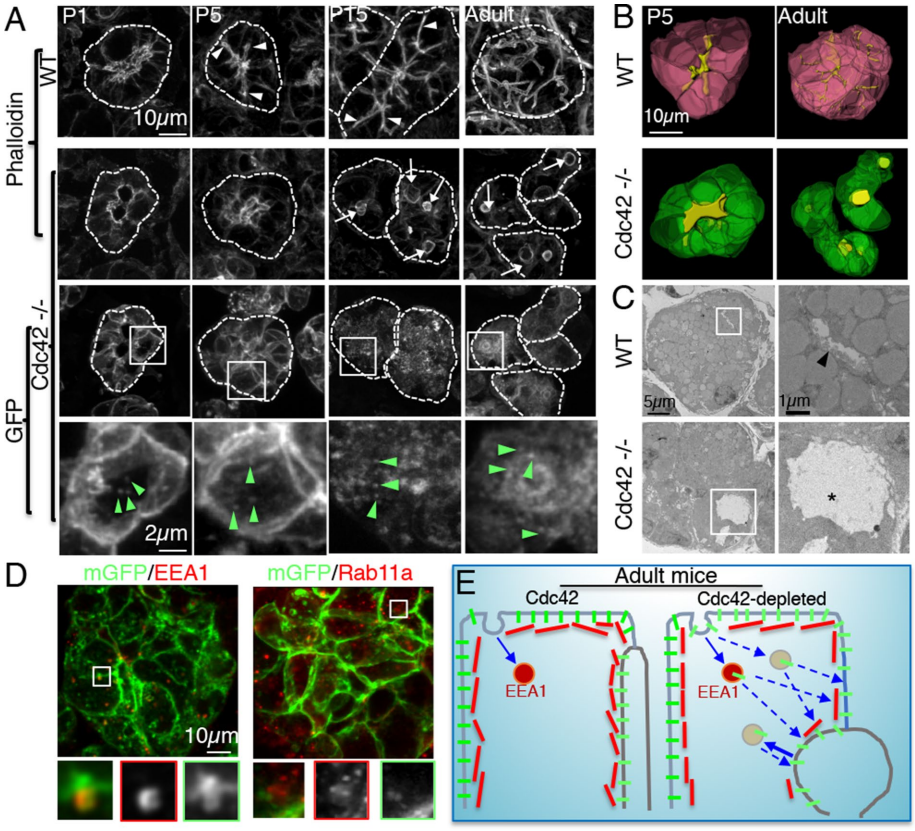

FIGURE 4: Cdc42 depletion impairs the formation of IC postnatally. (A–D) The SMGs of either $Cdc42^{fl/fl\text{-}mT/mG}$ (WT) or $Cdc42^{fl/fl\text{-}mT/mG}$/ACID-Cre mice ($Cdc42^{-/-}$) were excised at P1, P5, P15, and week 28 (Adult). (A, B) Samples were labeled with phalloidin and Z-stacks were acquired by confocal microscopy, as described in *Materials and Methods*. (A) Maximal projections of the SMGs. Arrowheads and arrows highlight developed IC and involuted central canaliculi labeled with phalloidin (top panels). Bottom panels show mGFP vesicles in the cytoplasm (insets, green arrowheads). Dotted lines show the outline of acini. (B) Volume rendering of acini. (C) EM micrograph of the SMG acini of WT (top panels) and $Cdc42^{-/-}$ mice (bottom panels). Insets, the arrowhead and asterisk show an IC and lumen, respectively. (D) SMGs of $Cdc42^{-/-}$ mice were processed for immunofluorescence and labeled with antibodies directed against either EEA1 (bottom panels) or Rab11a (right panels). (E) Proposed model.

bottom panels, and Supplemental Movie S5), similar to what was previously reported (Martin-Belmonte *et al.*, 2007; Kesavan *et al.*, 2009; Sakamori *et al.*, 2012). These represent, most likely, the final stage of the involution of the central lumens, as they were functionally connected to the ductal system (Supplemental Figure S4F and Supplemental Movie S6). Electron microscopy revealed that in the adult $Cdc42^{fl/fl}$-ACID-Cre mice the central luminal structures had reduced microvilli bulging into the lumen when compared with control mice (Figure 4C), a phenotype that was reported in the liver of $Cdc42^{-/-}$ mice (van Hengel *et al.*, 2008). Finally, we observed the progressive accumulation of mGFP-labeled vesicles that were not detected under control conditions (Figure 4A, bottom panels, green arrowheads). Similar to what was observed in the adult mice, these mGFP-labeled vesicles were labeled by EEA1 but not Rab11a (Figure 4D and insets), thus indicating that the Cdc42 negatively regulate endocytosis during development, as well.

Here we show that in vivo Cdc42 plays a fundamental role in maintaining the apical lumen in adult mice and in controlling its postnatal development. Cdc42 has been already described to regulate these processes in other organs and in cell cultures (Martin-Belmonte *et al.*, 2007; van Hengel *et al.*, 2008; Kesavan *et al.*, 2009; Sakamori *et al.*, 2012) by controlling polarity complexes, actin cytoskeleton, and membrane trafficking. Not surprisingly, we found that depletion of Cdc42 resulted in the loss of PAR6, as shown in mammalian epithelial cell culture and *Drosophila* epithelia (Harris and Tepass, 2010). However, whereas in vitro Cdc42 has been shown to enhance endocytic pathways via the regulation of the actin cytoskeleton (Georgiou *et al.*, 2008; Leibfried *et al.*, 2008; Sathe *et al.*, 2018), in the acinar cells of salivary glands in vivo we found that it negatively regulates this process. Indeed, down-regulation of Cdc42 induced a robust internalization of the membrane-targeted reporter mGFP, which is localized at both the basolateral and apical PM under control conditions. Resident basolateral, apical, or junctional proteins were not affected. However, although we did not observe any gross alteration in the morphology of the early, late, or recycling endosomal compartments, we cannot exclude the possibility that the lack of Cdc42 could also affect intracellular sorting and/or the late stage of recycling (i.e., fusion with the PM), thus resulting in the accumulation of endocytic vesicles.

Our findings raise the intriguing possibility that Cdc42, in addition to positively regulating membrane trafficking pathways from and to the APM, it may also prevent the internalization of selected proteins and lipids, which do not possess specific trafficking signals. Therefore, the enlarged canaliculi and the increase in the length of the apical–lateral border elicited by the down-regulation of Cdc42 could be explained by an unbalance of trafficking events, which result in a net increase of the delivery of internalized membranes to both sites (Figure 4E).

Whether this phenotype is related to a defect in the assembly of F-actin at the PM is still to be determined. Because cortical actin has been proposed to work as a functional barrier to prevent membrane fusion (Trifaro *et al.*, 2008), reduced levels of F-actin at the IC could result in an increase in constitutive exocytic fusion events. This could account for the increase in the IC surface area. In addition, cortical actin has been shown to control various steps of endocytosis by regulating, for example, membrane tension at the PM (Boulant *et al.*, 2011) or vesicle scission (Kaksonen *et al.*, 2005; Romer *et al.*, 2010). Although in yeast F-actin positively regulates the internalization process, in mammals it is dependent on the cell type and the specific endocytic pathway (Goode *et al.*, 2015; Hinze and Boucrot, 2018). Therefore, it is conceivable that in the salivary acinar cells in vivo inhibition of Cdc42-mediated F-actin assembly may simultaneously inhibit selected endocytic pathways and enhance others, as previously shown in *Drosophila* (Harris and Tepass, 2008). This applies to the APM of Cdc42-depleted acinar cells, where we detected reduced levels of F-actin. Vesicles internalized from the IC may be delivered to the adjacent lateral membrane, thus contributing to the increase in size of the apical–lateral border. However, at the basal membrane Cdc42 may control endocytosis through a different mechanism, because the F-actin levels were not affected by Cdc42

depletion. Finally, when Cdc42 was ablated at late embryonic stages, the canaliculi did not form but the increase in endocytic activity was still observed, thus suggesting that Cdc42 negatively regulates endocytosis during development, as well.

In conclusion, this study reveals an additional role of Cdc42 in regulating membrane trafficking in vivo and underscores the value of ISMic in live rodents to investigate the dynamics of membrane remodeling under physiological conditions. Our findings will lead us to address several mechanistic questions on the relationship among signaling, actin cytoskeleton, and membrane trafficking during PM homeostasis in vivo. Specifically, we are poised to further define the nature of the Cdc42-dependent endocytic pathways implicated in this process and to elucidate the machinery operating downstream from Cdc42 both at the apical and the basolateral membrane.

MATERIALS AND METHODS

Animals and procedures

All experiments were approved by the National Institute of Dental and Craniofacial Research (NIDCR, National Institutes of Health, Bethesda, MD) and National Cancer Institute (NCI, National Institutes of Health, Bethesda, MD) Animal Care and Use Committee. mT/mGFP mice were purchased from Jackson Laboratory (Bar Harbor, ME). $Cdc42^{fl/fl}$, $RhoA^{fl/fl}$, and $Rac1^{fl/fl}$ mice were a generous gift of Y. Zheng (Cincinnati Children's Hospital Medical Center). ACID-Cre (AQP5-Cre) mice were a generous gift of Z. Borok (University of Southern California). These mice were crossed according to Supplemental Figures S1 and S4, and PCR was used to confirm their genotypes. All the mice (males and females) used in this study weighed 20–40 g. Mice were anesthetized by an intraperitoneal injection of a mixture of ketamine (100 mg/kg) and xylazine (20 mg/kg).

Adenovirus transfection into the mouse submandibular salivary glands

Adeno-Cre was prepared using the ViraPower Adenoviral Expression System as described in Milberg *et al.*, 2017 (Life Technologies, Carlsbad, CA). To inject the Adeno-Cre into the SMG, anesthetized mice were positioned in a custom-made device (Masedunskas *et al.*, 2013) that allowed holding the mouth of the mice open under a stereomicroscope. A PE-8 cannula (Strategic Applications, Libertyville, IL) was connected to a 31-gauge sterile insulin syringe loaded with Adeno-Cre (~10^9–10^{10} particles/gland in sterile saline) through a MicroFil Custom 35 gauge needle (World Precision Instruments, Sarasota, FL). The cannula was inserted in the main SMG duct (Wharton's duct) located below the tongue and stabilized with commercial super glue. Atropine (0.5 mg/kg) was injected subcutaneously 10 min before Adeno-Cre injection to prevent fluid secretion. The Adeno-Cre (total volume per gland, 20 µl) was injected using a PHD Ultra Nanomite syringe pump (Harvard Apparatus, Holliston, MA) at a flow rate of 5 µl/min. The cannula was removed 10 min after the injection. After recovery from anesthesia, mice were allowed to recover and placed back in their cages.

Indirect immunofluorescence

Immunostaining for Adeno-Cre transfected gland and for ACID-Cre–expressing gland was performed in nonfrozen section and in cryosections, respectively. Primary and secondary antibodies used in this study are listed in Table 1. SMGs were fixed by cardiac perfusion using a solution consisting of 4% formaldehyde in 0.2 M HEPES buffered at a pH of 7.3 and postfixed overnight. For nonfrozen section, fixed glands were sliced using a vibratome (Leica; VT1000s, 150–200 µm thickness). For cryosections, glands were placed in optimum cutting temperature compound (Sakura Finetek USA, Torrance, CA), snap-frozen in 2-methylbutane on liquid nitrogen, and cut using a cryostat (Leica; CM3050S, 10 µm thickness). Immunostaining was performed as follows. Samples were incubated 1) in 10% fetal bovine serum and 0.02% saponin in fetal bovine serum (blocking solution) for 30–45 min at room temperature, 2) with primary antibodies in blocking solution at 4°C for either 2 d (nonfrozen section) or overnight (cryosections), 3) with secondary antibodies in blocking solution at 4°C either overnight (nonfrozen section) or for 30 min (cryosection), and 4) if needed, with either phalloidin or Hoechst, for 30–60 min at room temperature. Finally, samples were mounted on a glass slide and covered with a #1.5 coverslip.

ISMic

In anesthetized mice, SMGs were exposed by a small longitudinal incision in the submandibular region. Connective tissue was separated from the glands without injuring the parenchyma, and the exposed glands were gently pulled out, taking care to avoid tissue damage. Mice were placed on the preheated stage of a confocal microscope (see next section) and covered with a heated pad (37–38°C) to maintain the body temperature, as previously described (Masedunskas *et al.*, 2013). The externalized SMGs were accommodated on a coverslip mounted on the stage above the objective and constantly moistened with a carbomer-940-based gel (Snowdrift Farm, Tucson, AZ; Masedunskas and Weigert, 2008). The glands and the body of the animal were immobilized using custom-made holders, as previously shown (Masedunskas *et al.*, 2011a).

To deliver 3 kDa Cascade Blue Dextran (Thermo Fisher Scientific, Waltham, MA), anesthetized mice were cannulated first, and the SMGs exposed, as described above. Mice were placed under the microscope and imaged while the injections were performed with the pump (see above) at a flow rate of 300–500 nl/min.

Microscope and imaging parameters

ISMic and indirect immunofluorescence were performed by a point-scanning IX81 inverted confocal microscope equipped with a Fluoview 1000 scanning head (Olympus America). All images were acquired using a Plan Apo 60× NA 1.42 oil immersion objective (Olympus America). Fluorophores were imaged using the appropriate lasers as required by their excitation spectra (laser excitation 405, 488, 561, or 633 nm). Fluorophores with slightly overlapping emission ranges were imaged using the "sequential" scanning mode to avoid bleed-through. The optimal focal plane for imaging the acinar cells was set at ~15 µm below the surface of the gland, as determined by visualization of the collagen capsule that surrounded the acinar cells. For ISMic of exocytosis and dextran delivery, the acquisition speed was set at 2 and 10 s/frame, respectively. And the pinhole was optimally set to 0.9 µm. Z-stacks were acquired with a step size of 0.50–1.00 µm. During acquisition, XYZ drift was manually corrected.

Tracking analysis

To enhance the visualization of the vesicles, the brightness of the original movie was adjusted so that the threshold was 50% of the maximum original brightness of the whole movie and the grayscale gamma was set to 0.6. To manually track the vesicles, a customized MATLAB script was executed to display the movie frame by frame with pseudocolor equal-brightness contour to emphasize the shape of the objects. The displayed frame allowed one to click on the image to select the position of the object identified as a vesicle by the eyes. After the selection, the script automatically recorded the selected position and switched the image to the next frame to select the position of the same vesicle in the next frame.

Antibody/probe	Species	Source	Catalog no./ref.	Dilution
Cdc42	Rabbit	Thermo Fisher Scientific	PA1-092X	1:50
Par6 (PARD6B)(H-64)	Rabbit	Santa Cruz	sc-67392	1:100
Aquaporin 5	Rabbit	Alomone Labs	AQP-005	1:50 (nonfrozen)
				1:200 (cryosection)
NKCC1 (N-16)	Goat	Santa Cruz	sc-21545	1:100
ZO-1 (clone R40.76)	Rat	Gift from J. M. Anderson (National Institutes of Health)	Anderson *et al.*, 1988	1:200 (cryosection)
				1:100 (cryosection)
Rab11a	Rabbit	Thermo Fisher Scientific	71-5300	
EEA1	Rabbit	Cell Signaling	32885	1:50 (nonfrozen)
				1:100 (cryosection)
LAMP1	Rabbit	Cell Signaling	15665	1:100 (cryosection)
TGN46	Rabbit	Abcam	Ab16059	1:100 (cryosection)
VAMP4	Rabbit	Sigma	V4514	1:100 (cryosection)
LC3	Rabbit	Cell Signaling	3868S	1:100 (cryosection)
E-cadherin	Goat	R&D	AF648	1:50
Alexa Fluor 594-Phalloidin			A12381	
Alexa Fluor 647-Phalloidin			A22287	
Phalloidin-iFluor 405		Abcam	ab176752	1:100

TABLE 1: Antibodies used in this study.

Transmission electron microscopy

The gland tissue was excised and fixed for 90 min in 2% glutaraldehyde, 2% formaldehyde (Electron Microscopy Sciences, Hatfield, PA), in 0.1 phosphate buffer (pH 7.2), postfixed in aqueous 1% osmium tetroxide, block stained with 1% uranyl acetate, dehydrated in graded ethanol solutions, and embedded in EMbed-812 (Electron Microscopy Sciences). Thin sections were stained with uranyl acetate and lead citrates and then examined on a JEM-1200EX (JEOL) transmission electron microscope (accelerating voltage 80 keV) equipped with an AMT 6-megapixel digital camera (Advanced Microscopy Techniques Corp.).

Image analysis and quantitation

For measurement of fluorescence intensity, images were acquired by confocal microscopy using the same laser power and detector settings for control and Cdc42-depleted cells. Images with the highest fluorescence intensity were selected from Z-stacks, and the contours of the apical membranes, basolateral membranes, and fused secretory granules were traced manually. Total fluorescence intensity was measured using ImageJ and normalized for the area of the structure. For Adeno-Cre transfected glands, fluorescence intensities of Cdc42-depleted cells were compared with those of neighboring control cells. For quantifications of Cdc42 levels, immunofluorescence levels in Cre-expressing cells were normalized to that of neighboring control cells. Statistical significance was calculated using the paired or unpaired Student's *t* test. Paired tests were used when immunofluorescence (IF) was measured in cells within the same acinus. The volume rendering and measurement of surface area were performed with Imaris (Bitplane, Belfast, United Kingdom) using the isosurface tool. The structure of the IC and cell shape were traced according to fluorescence of phalloidin and of mT/mGFP, respectively. The time-lapse movies from ISMic were processed as described elsewhere (Milberg *et al.*, 2017). Prior to quantification, motion artifacts created during ISMic was stabilized using the Stackreg plug-in in Fiji (National Institutes of Health, Bethesda, MD). In mice expressing the mT/mGFP reporter, the diameter of fused secretory granules was estimated from the circular profiles at the APM labeled by either mT or mGFP. Diameters were measured in time series from the frame the profiles of the granules were clearly visible. Images were analyzed and assembled in Fiji and Imaris. Data analysis was done in Prism (GraphPad, San Diego, CA) and Excel (Microsoft, Redmond, WA).

ACKNOWLEDGMENTS

This research was supported by the Intramural Research Program of the National Institutes of Health, National Cancer Institute, Center for Cancer Research, and National Institute of Dental and Craniofacial Research. We thank Julie Donaldson for critical reading of the manuscript; Zea Borok, Edward Crandall, and Peter Flodby for providing the ACID mice; James M. Anderson for providing the ZO-1 antibody; Cameron Keshavarz and Erin Stempinski for assistance during the electron microscopy (EM) preparation; and Yoshikatsu Sato and Yasuhiro Kamei for helping with the image processing.

REFERENCES

Anderson JM, Stevenson BR, Jesaitis LA, Goodenough DA, Mooseker MS (1988). Characterization of ZO-1, a protein component of the tight junction from mouse liver and Madin-Darby canine kidney cells. J Cell Biol 106, 1141–1149.

Apodaca G (2010). Opening ahead: early steps in lumen formation revealed. Nat Cell Biol 12, 1026–1028.

Bai Z, Grant BD (2015). A TOCA/CDC-42/PAR/WAVE functional module required for retrograde endocytic recycling. Proc Natl Acad Sci USA 112, E1443–E1452.

Balklava Z, Pant S, Fares H, Grant BD (2007). Genome-wide analysis identifies a general requirement for polarity proteins in endocytic traffic. Nat Cell Biol 9, 1066–1073.

Boulant S, Kural C, Zeeh JC, Ubelmann F, Kirchhausen T (2011). Actin dynamics counteract membrane tension during clathrin-mediated endocytosis. Nat Cell Biol 13, 1124–1131.
Bryant DM, Datta A, Rodríguez-Fraticelli AE, Peränen J, Martín-Belmonte F, Mostov KE (2010). A molecular network for de novo generation of the apical surface and lumen. Nat Cell Biol 12, 1035–1045.
Bryant DM, Mostov KE (2008). From cells to organs: building polarized tissue. Nat Rev Mol Cell Biol 9, 887–901.
Chen L, Liao G, Yang L, Campbell K, Nakafuku M, Kuan C-YY, Zheng Y (2006). Cdc42 deficiency causes Sonic hedgehog-independent holoprosencephaly. Proc Natl Acad Sci USA 103, 16520–16525.
Etienne-Manneville S (2004). Cdc42—the centre of polarity. J Cell Sci 117, 1291–1300.
Flodby P, Borok Z, Banfalvi A, Zhou B, Gao D, Minoo P, Ann DK, Morrisey EE, Crandall ED (2010). Directed expression of Cre in alveolar epithelial type 1 cells. Am J Respir Cell Mol Biol 43, 173–178.
Georgiou M, Marinari E, Burden J, Baum B (2008). Cdc42, Par6, and aPKC regulate Arp2/3-mediated endocytosis to control local adherens junction stability. Curr Biol 18, 1631–1638.
Goode BL, Eskin JA, Wendland B (2015). Actin and endocytosis in budding yeast. Genetics 199, 315–358.
Harris KP, Tepass U (2008). Cdc42 and Par proteins stabilize dynamic adherens junctions in the *Drosophila* neuroectoderm through regulation of apical endocytosis. J Cell Biol 183, 1129–1143.
Harris KP, Tepass U (2010). Cdc42 and vesicle trafficking in polarized cells. Traffic 11, 1272–1279.
Hinze C, Boucrot E (2018). Local actin polymerization during endocytic carrier formation. Biochem Soc Trans 46, 565–576.
Jaffe AB, Kaji N, Durgan J, Hall A (2008). Cdc42 controls spindle orientation to position the apical surface during epithelial morphogenesis. J Cell Biol 183, 625–633.
Joberty G, Petersen C, Gao L, Macara IG (2000). The cell-polarity protein Par6 links Par3 and atypical protein kinase C to Cdc42. Nat Cell Biol 2, 531–539.
Kaksonen M, Toret CP, Drubin DG (2005). A modular design for the clathrin- and actin-mediated endocytosis machinery. Cell 123, 305–320.
Kamei M, Saunders WB, Bayless KJ, Dye L, Davis GE, Weinstein BM (2006). Endothelial tubes assemble from intracellular vacuoles in vivo. Nature 442, 453–456.
Kesavan G, Sand FW, Greiner TU, Johansson JK, Kobberup S, Wu X, Brakebusch C, Semb H (2009). Cdc42-mediated tubulogenesis controls cell specification. Cell 139, 791–801.
Leibfried A, Fricke R, Morgan MJ, Bogdan S, Bellaiche Y (2008). *Drosophila* Cip4 and WASp define a branch of the Cdc42-Par6-aPKC pathway regulating E-cadherin endocytosis. Curr Biol 18, 1639–1648.
Martin-Belmonte F, Gassama A, Datta A, Yu W, Rescher U, Gerke V, Mostov K (2007). PTEN-mediated apical segregation of phosphoinositides controls epithelial morphogenesis through Cdc42. Cell 128, 383–397.
Masedunskas A, Sramkova M, Parente L, Sales KU, Amornphimoltham P, Bugge TH, Weigert R (2011a). Role for the actomyosin complex in regulated exocytosis revealed by intravital microscopy. Proc Natl Acad Sci USA 108, 13552–13557.
Masedunskas A, Sramkova M, Parente L, Weigert R (2013). Intravital microscopy to image membrane trafficking in live rats. Methods Mol Biol 931, 153–167.
Masedunskas A, Sramkova M, Weigert R (2011b). Homeostasis of the apical plasma membrane during regulated exocytosis in the salivary glands of live rodents. BioArchitecture 1, 225–229.
Masedunskas A, Weigert R (2008). Intravital two-photon microscopy for studying the uptake and trafficking of fluorescently conjugated molecules in live rodents. Traffic 9, 1801–1810.
Matsuzaki T, Suzuki T, Koyama H, Tanaka S, Takata K (1999). Aquaporin-5 (AQP5), a water channel protein, in the rat salivary and lacrimal glands: immunolocalization and effect of secretory stimulation. Cell Tissue Res 295, 513–521.
Melendez J, Grogg M, Zheng Y (2011). Signaling role of Cdc42 in regulating mammalian physiology. J Biol Chem 286, 2375–2381.
Melendez J, Liu M, Sampson L, Akunuru S, Han X, Vallance J, Witte D, Shroyer N, Zheng Y (2013). Cdc42 coordinates proliferation, polarity, migration, and differentiation of small intestinal epithelial cells in mice. Gastroenterology 145, 808–819.
Milberg O, Shitara A, Ebrahim S, Masedunskas A, Tora M, Tran DT, Chen Y, Conti MA, Adelstein RS, Ten Hagen KG, *et al*. (2017). Concerted actions of distinct nonmuscle myosin II isoforms drive intracellular membrane remodeling in live animals. J Cell Biol 216, 1925–1936.
Milberg O, Tora M, Shitara A, Takuma T, Masedunskas A, Weigert R (2014). Probing the role of the actin cytoskeleton during regulated exocytosis by intravital microscopy. Methods Mol Biol 1174, 407–421.
Morais-de-Sá E, Mirouse V, St Johnston D (2010). aPKC phosphorylation of bazooka defines the apical/lateral border in *Drosophila* epithelial cells. Cell 141, 509–523.
Muzumdar MD, Tasic B, Miyamichi K, Li L, Luo L (2007). A global double-fluorescent Cre reporter mouse. Genesis 45, 593–605.
O'Grady SM, Palfrey HC, Field M (1987). Characteristics and functions of Na-K-Cl cotransport in epithelial tissues. Am J Physiol 253, C177–C192.
Pirraglia C, Walters J, Myat MM (2010). Pak1 control of E-cadherin endocytosis regulates salivary gland lumen size and shape. Development 137, 4177–4189.
Pittet MJ, Weissleder R (2011). Intravital imaging. Cell 147, 983–991.
Rojas R, Ruiz WG, Leung SM, Jou TS, Apodaca G (2001). Cdc42-dependent modulation of tight junctions and membrane protein traffic in polarized Madin-Darby canine kidney cells. Mol Biol Cell 12, 2257–2274.
Romer W, Pontani LL, Sorre B, Rentero C, Berland L, Chambon V, Lamaze C, Bassereau P, Sykes C, Gaus K, *et al*. (2010). Actin dynamics drive membrane reorganization and scission in clathrin-independent endocytosis. Cell 140, 540–553.
Sakamori R, Das S, Yu S, Feng S, Stypulkowski E, Guan Y, Douard V, Tang W, Ferraris RP, Harada A, *et al*. (2012). Cdc42 and Rab8a are critical for intestinal stem cell division, survival, and differentiation in mice. J Clin Invest 122, 1052–1065.
Sathe M, Muthukrishnan G, Rae J, Disanza A, Thattai M, Scita G, Parton RG, Mayor S (2018). Small GTPases and BAR domain proteins regulate branched actin polymerisation for clathrin and dynamin-independent endocytosis. Nat Commun 9, 1–16.
Sramkova M, Masedunskas A, Parente L, Molinolo A, Weigert R (2009). Expression of plasmid DNA in the salivary gland epithelium: novel approaches to study dynamic cellular processes in live animals. Am J Physiol Cell Physiol 297, C1347–C1357.
Stevenson BR, Siliciano JD, Mooseker MS, Goodenough DA (1986). Identification of ZO-1: a high molecular weight polypeptide associated with the tight junction (zonula occludens) in a variety of epithelia. J Cell Biol 103, 755–766.
Suzuki A, Ohno S (2006). The PAR-aPKC system: lessons in polarity. J Cell Sci 119, 979–987.
Tamarin A, Sreebny LM (1965). The rat submaxillary salivary gland. A correlative study by light and electron microscopy. J Morphol 117, 295–352.
Tepass U (2012). The apical polarity protein network in *Drosophila* epithelial cells: regulation of polarity, junctions, morphogenesis, cell growth, and survival. Annu Rev Cell Dev Biol 28, 655–685.
Trifaro JM, Gasman S, Gutierrez LM (2008). Cytoskeletal control of vesicle transport and exocytosis in chromaffin cells. Acta Physiol (Oxf) 192, 165–172.
Tucker AS (2007). Salivary gland development. Semin Cell Dev Biol 18, 237–244.
Ueyama T, Sakaguchi H, Nakamura T, Goto A, Morioka S, Shimizu A, Nakao K, Hishikawa Y, Ninoyu Y, Kassai H, *et al*. (2014). Maintenance of stereocilia and apical junctional complexes by Cdc42 in cochlear hair cells. J Cell Sci 127, 2040–2052.
van Hengel J, D'Hooge P, Hooghe B, Wu X, Libbrecht L, De Vos R, Quondamatteo F, Klempt M, Brakebusch C, van Roy F (2008). Continuous cell injury promotes hepatic tumorigenesis in cdc42-deficient mouse liver. Gastroenterology 134, 781–792.
Walther RF, Pichaud F (2010). Crumbs/DaPKC-dependent apical exclusion of Bazooka promotes photoreceptor polarity remodeling. Curr Biol 20, 1065–1074.
Weigert R, Porat-Shliom N, Amornphimoltham P (2013). Imaging cell biology in live animals: ready for prime time. J Cell Biol 201, 969–979.
Willenborg C, Prekeris R (2011). Apical protein transport and lumen morphogenesis in polarized epithelial cells. Biosci Rep 31, 245–256.
Winter JF, Hopfner S, Korn K, Farnung BO, Bradshaw CR, Marsico G, Volkmer M, Habermann B, Zerial M (2012). *Caenorhabditis elegans* screen reveals role of PAR-5 in RAB-11-recycling endosome positioning and apicobasal cell polarity. Nat Cell Biol 14, 666–676.